Dispersed Nickel Phthalocyanine Molecules on Carbon Nanotubes as Cathode Catalysts for Li-CO$_2$ Batteries

Hongzhi Zheng, Huan Li, Zisheng Zhang, Xiaojun Wang, Zhan Jiang, Yirong Tang, Jibo Zhang, Benjamin Emley, Ye Zhang, Hua Zhou, Yan Yao,* and Yongye Liang*

The Li-CO$_2$ battery has great potential for both CO$_2$ utilization and energy storage, but its practical application is limited by low energy efficiency and short cycle life. Efficient cathode catalysts are needed to address this issue. Herein, this work reports on molecularly dispersed electrocatalysts (MDEs) of nickel phthalocyanine (NiPc) anchored on carbon nanotubes (CNTs) as the cathode catalyst for Li-CO$_2$ batteries. The dispersed NiPc molecules efficiently catalyze CO$_2$ reduction, while the conductive and porous CNTs networks facilitate CO$_2$ evolution reaction, leading to enhanced discharging and charging performance compared to the NiPc and CNTs mixture. Octa-cyano substitution on NiPc (NiPc-CN) further enhances the interaction between the molecule and CNTs, resulting in better cycling stability. The Li-CO$_2$ battery with the NiPc-CN MDE cathode shows a high discharge voltage of 2.72 V and a small discharging–charging potential gap of 1.4 V, and can work stably for over 120 cycles. The reversibility of the cathode is confirmed by experimental characterizations. This work lays a foundation for the development of molecular catalysts for Li-CO$_2$ battery cathodes.

1. Introduction

CO$_2$ capture, storage, and utilization have attracted tremendous attention due to growing problems caused by excessive utilization of fossil fuels.[1–3] New energy storage devices are anticipated for the utilization of renewable energy and alleviation of the greenhouse effect. Metal-CO$_2$ battery is a promising technology for the efficient conversion between chemical energy and electrical energy with CO$_2$ as an energy carrier.[4] The Li-CO$_2$ battery is more favored because of its high discharge voltage ($\approx$2.8 V) and high specific energy densities (1876 Wh kg^{-1}).[5–7] It is advantageous as the power supply on some particular occasions with high concentration of CO$_2$.[8] The reversible redox reactions between CO$_2$ and Li$_2$CO$_3$ are key for the discharge–charge processes. Unfortunately, the slow reaction kinetics of CO$_2$ and the insulation nature of Li$_2$CO$_3$ covered on cathode surface usually result in the distressing issue of large charge–discharge overpotential.[4,5,9] Besides, some parasitic catalyst problems such as the active site degradation or detachment from the conductive substrate during charge–discharge cycles could inevitably cause serious decay to battery life.[5,10–12] Therefore, it is highly desirable but challenging to develop efficient and stable cathode catalyst materials, which can efficiently catalyze the reduction of CO$_2$ and the decomposition of Li$_2$CO$_3$.

Until now, several types of cathode catalysts have been developed for Li-CO$_2$ batteries. Precious metal-based catalysts, such as RuRh,[13] Ir,[14,16] Ru,[15,17] and RuO[18] can exhibit relatively high catalytic activities with lower voltage gaps (<1.4 V) and long cycling life (> 100 cycles). However, their practical applications are limited by high cost and scarcity of precious metals. Recently, first row transition metal-based catalysts were also reported to show good performances. A nitrogen-doped 3D porous graphene catalyst modified with highly dispersed Ni nanoparticles could show strong interaction with Li$^+$ and CO$_2$.[19] Wang et al. reported

H. Zheng, H. Li, Z. Zhang, Z. Jiang, Y. Tang, Y. Liang
Department of Materials Science and Engineering
Southern University of Science and Technology
Shenzhen, Guangdong 518055, China
E-mail: liangyy@sustech.edu.cn
H. Zheng, X. Wang, J. Zhang, B. Emley, Y. Zhang, Y. Yao
Department of Electrical and Computer Engineering and Texas Center for Superconductivity
University of Houston
Houston, TX 77204, USA
E-mail: yyao4@uh.edu

Z. Zhang
Department of Chemistry and Biochemistry
University of California, Los Angeles
Los Angeles, California 90095, USA
H. Zhou
X-Ray Science Division
Advanced Photon Source
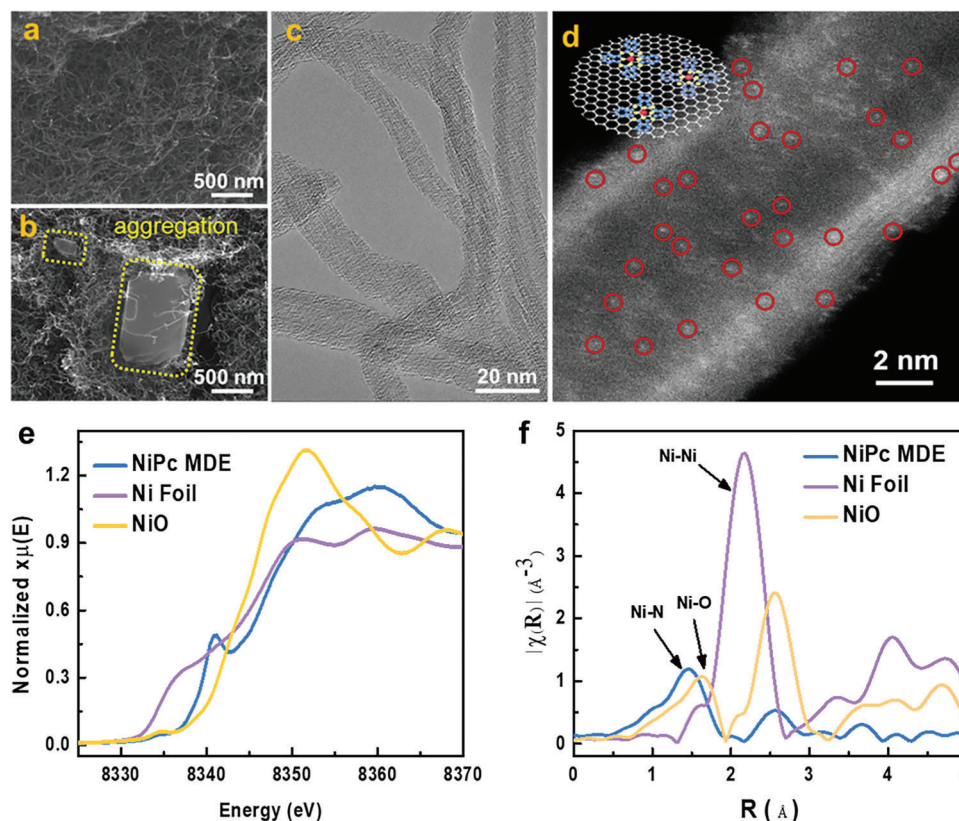Argonne National Laboratory
Lemont, IL 60439, USA

Figure 1. Characterization of NiPc MDE and NiPc+CNTs. SEM images of a) NiPc MDE and b) NiPc+CNTs. c) TEM image and d) aberration-corrected HAADF-STEM image of NiPc MDE (inset shows the schematic of NiPc molecules anchored on CNTs). e) Ni K-edge XANES and f) EXAFS of NiPc MDE, NiPc, Ni foil and NiO.

Mn organic frameworks for Li-CO$_2$ batteries which showed remarkable discharge capacity.[20] Cheng et al. reported a series of metal-N$_4$ functionalized graphene electrocatalysts and found that the SACr@NG/PCF catalyst had a small voltage gap of 1.39 V.[21]

As a kind of promising electrocatalyst with the metal-N$_4$ active center, metal phthalocyanines (MPcs) have many advantages such as well-defined structure, easy tunability, good stability, etc. They have shown good electrocatalytic performance for the CO$_2$ reduction reaction (CO$_2$RR) in aqueous solutions.[22–25] Recently, cobalt polyphthalocyanine (CoPPc) was prepared as the cathode catalyst for Li-CO$_2$ batteries, showing a discharge capacity of 13 600 mAh g^{-1} and operation of 50 cycles.[26] However, phthalocyanine molecules are not conductive and tend to aggregate in heterogeneous conditions, resulting in ineffective electron transport and limited diffusion of CO$_2$ and electrolytes to active sites.

Herein, we introduced molecularly dispersed electrocatalysts (MDEs) for Li-CO$_2$ battery cathode. These MDEs are constructed by anchoring nickel phthalocyanine (NiPc) (Figure S1, Supporting Information) on multiwalled carbon nanotubes (CNTs), which were used as carbon substrates in Li-CO$_2$ batteries due to their excellent conductivity, large specific surface area and porous network structure.[6,27,28] NiPc MDE can fully display the intrinsic activity of NiPc for CO$_2$RR, and CNTs provide a high surface area and porous network, facilitating the decomposition of Li$_2$CO$_3$. Thus, the NiPc MDE cathode exhibits higher discharge voltage, lower charge voltage, and larger discharge capacity than those of

the battery with the physical mixture of NiPc and CNTs (denoted as NiPc+CNTs). However, NiPc MDE battery shows inferior cycling stability due to the dissolution of NiPc from the cathode. To solve this problem, CN groups are introduced to NiPc (Figure S1, Supporting Information) to enhance the interaction between molecules and CNTs. The afforded NiPc-CN MDE cathode shows better activity and stability. Further, the reversibility of the whole battery system is verified by a series of experimental characterizations.

2. Results and Discussion

NiPc MDE was prepared via a solution sonication approach (Experimental Section). The Ni content in NiPc MDE hybrid is ≈0.7 wt% (Table S1, Supporting Information). The deposition of NiPc MDE on the substrate shows a nanoporous network connected with ≈15 nm diameter nanotubes (**Figure 1**a). In contrast, the physical mixture, NiPc+CNTs shows obvious molecular aggregation at the sub-micron size scale (Figure 1b). The image of transmission electron microscopy (TEM) shows the 1D morphology of NiPc MDE without aggregation of nanoparticles, which validates the SEM results (Figure 1c). The aberration-corrected high-angle annular dark-field scanning (HAADF) TEM further shows the presence of isolated bright spots (surrounded by red circles) on CNTs (Figure 1d), suggesting the modification of heavier atoms on the carbon framework. As Ni is the only substantially

heavier element in NiPc MDE, the result suggests that NiPc molecules are distributed on the surface of multi-walled CNTs without significant molecular aggregation. The EDS mappings show that C, N, and Ni are located in the carbon nanotubes skeleton region, suggesting that NiPc molecules are distributed on the surface of CNTs in NiPc MDE (Figure S2, Supporting Information). In Figure 1e, the K-edge X-ray absorption near-edge structure spectrum (XANES) of NiPc MDE is highly similar to that of neat NiPc molecule, showing an apparent pre-edge peak at 8342 eV corresponds to the typical $Ni-N_4$ configuration.[29] In the corresponding extended X-ray absorption fine structure (EXAFS) spectrum (Figure 1f), NiPc MDE displays a dominant peak at 1.45 Å arising from Ni–N bond coordination, consistent with the definite NiPc structure.[30,31] The Ni-Ni coordination peak at 2.15 Å is not found in NiPc MDE, suggesting Ni atoms on NiPc MDE are isolated, agreeing well with the TEM results.

In order to evaluate the comprehensive performance of NiPc MDE in $Li-CO_2$ battery, we assembled the battery as shown in **Figure 2**a (Experimental Section). NiPc MDE was coated on the carbon fiber paper substrate as the cathode. Glass fiber was used as the separator. Lithium bis(trifluoromethane)sulfonimide (LiTFSI) in tetramethylene glycol dimethyl ether (TEGDME) (G4) was used as the electrolyte. The electrochemical behavior of NiPc MDE was first studied by cyclic voltammetry (CV) (Figure 2b). Negligible currents are observed for NiPc MDE under an Ar atmosphere within the range of 2.2–4.5 V. Under CO_2 conditions, NiPc MDE exhibits obvious cathodic currents below ≈2.85 V and anodic currents above ≈3.51 V, showing good electrochemical catalytic performance for the CO_2 reduction and evolution reactions. In contrast, the control sample of NiPc+CNTs shows lower reduction and oxidation currents. There are aggregated nanoparticles of NiPc molecules in NiPc+CNTs (Figure 1b), which causes fewer exposed active sites and poorer electron transport, consequently resulting in much inferior electrocatalytic activity. The CNTs sample shows much smaller reduction currents than those of NiPc MDE, indicating that dispersed NiPc molecules on CNTs are in charge of the reduction catalytic activity in NiPc MDE. It is noteworthy to note that in the voltage window range of 3.5–4.5 V, CNTs exhibit a slightly higher oxidation current than NiPc+CNTs, which indicates that CNTs have a certain oxidation performance. This also indicates that the aggregated phthalocyanine molecules could not only mask their own active centers but also weaken the oxidation performance of CNTs. Without the influence of NiPc aggregation, NiPc MDE also shows a larger oxidation current, possibly due to more reduction products for oxidation.

The discharge–charge profiles displayed in Figure 2c indicate that NiPc MDE delivers a discharge voltage platform of ≈2.67 V, substantially higher than NiPc+CNTs (2.58 V) and CNTs (2.54 V). The charge profiles of NiPc MDE and CNTs are similar, both are lower than that of NiPc+CNTs, indicating the importance of CNTs conductive network for CO_2 evolution reaction (CO_2ER). The deep discharge measurement indicates that the NiPc MDE cathode exhibits the highest discharge capacity of 10 800 mAh g^{-1} at the current density of 200 mA g^{-1}, while the CNTs and NiPc+CNTs only reach ≈6000 and 8000 mAh g^{-1}, respectively (Figure 2d). Although the CNTs, NiPc MDE, and NiPc+CNTs samples show similar pore distribution and approximate Brunauer–Emmett–Teller (BET) surface area of 155, 146,

and 130 m^2 g^{-1}, respectively, their battery performance varies greatly (Figures S3 and S4, Supporting Information). It suggests that the fully exposed $Ni-N_4$ sites could effectively enhance the CO_2 catalysis during the discharge process. The cycling performance was investigated and the results are shown in Figure 2e. The CNTs and NiPc+CNTs cathodes show poor stability with a significant voltage gap increase from 1.8 to 2.8 V within the first 8 cycles. Although NiPc MDE with higher electrocatalytic activity shows better battery stability when compared with NiPc+CNTs and CNT, its voltage gap increases from 1.48 to 1.86 V in the first 8 cycles.

To explore the reasons for the poor battery stability, we disassembled the battery after 20 cycles of operation. The separator shows obvious blue color, which is the characteristic color of NiPc in organic solvent (Figure 3a(i)). The Ultraviolet-visible spectrum measurement proves that the blue particles on the separator are NiPc molecules (Figure S5, Supporting Information). It implies that the NiPc molecules were detached from CNTs side walls from NiPc MDE and deposited on the separator, due to the solvation ability of TEGDME in the electrolyte, resulting in the instability issue of the NiPc MDE cathode. We undertook DFT calculations for the interaction between NiPc and CNTs side wall and found that the adsorption energy of NiPc on CNTs surface is −2.47 eV (Figure 3b).[32] Interestingly, it is further found that the β-octa cyano-substituted NiPc (NiPc-CN) (Figure S1, Supporting Information) can afford stronger interaction with CNTs side wall with the adsorption energy of −3.52 eV (Figure 3c). To verify our anticipation, NiPc-CN MDE was synthesized and a series of characterizations confirm its similar structure to NiPc MDE (Figures S6 and S7, Supporting Information). Then NiPc-CN MDE was investigated as a cathode catalyst. After 100 cycles of operation, we disassembled the battery and found no characteristic color of phthalocyanine on the separator (Figure 3a(ii)). The weaker interaction between NiPc and CNTs could result in the dissolution of NiPc molecules in the TEGDME solvent during the battery operation, leading to the loss of catalytic activity (Figure 3d). In contrast, the stronger interactions between NiPc-CN and CNTs ensure the firm anchoring of molecules on CNTs, affording stable operation (Figure 3e).

The comprehensive performance of the NiPc-CN MDE cathode was further evaluated. As shown in Figure S8, Supporting Information, the cathode current of NiPc-CN MDE is higher than that of NiPc MDE, while the anode current is very similar to that of NiPc MDE. These results indicate that cyano substitution can promote the CO_2RR activity of NiPc, while the CO_2ER performance of CNTs is not affected by the change of molecular structure. **Figure 4**a shows the discharge–charge curves of ~~the~~ NiPc-CN MDE cathode. Impressively, it exhibits a higher discharge voltage of 2.72 V and a low charge voltage of 4.11 V, which are superior to those of NiPc MDE (2.67 and 4.18 V, respectively). In addition, the $Li-CO_2$ batteries of ~~the~~ NiPc-CN MDE cathode with different Ni amounts were investigated (Figure S9, Supporting Information). Among them, the 0.7 wt% sample exhibits the smallest potential gap of 1.39 V with the highest discharge potential (2.72 V). NiPc-CN MDE demonstrates a high discharge capacity of 18 000 mA hg^{-1}, which is among the highest for the reported non-noble transition metal-based catalysts (Figure 4b, Table S1, Supporting Information). In Figure 4c, the discharge terminal voltages of NiPc-CN MDE are 2.72, 2.65, 2.52, and 2.50 V
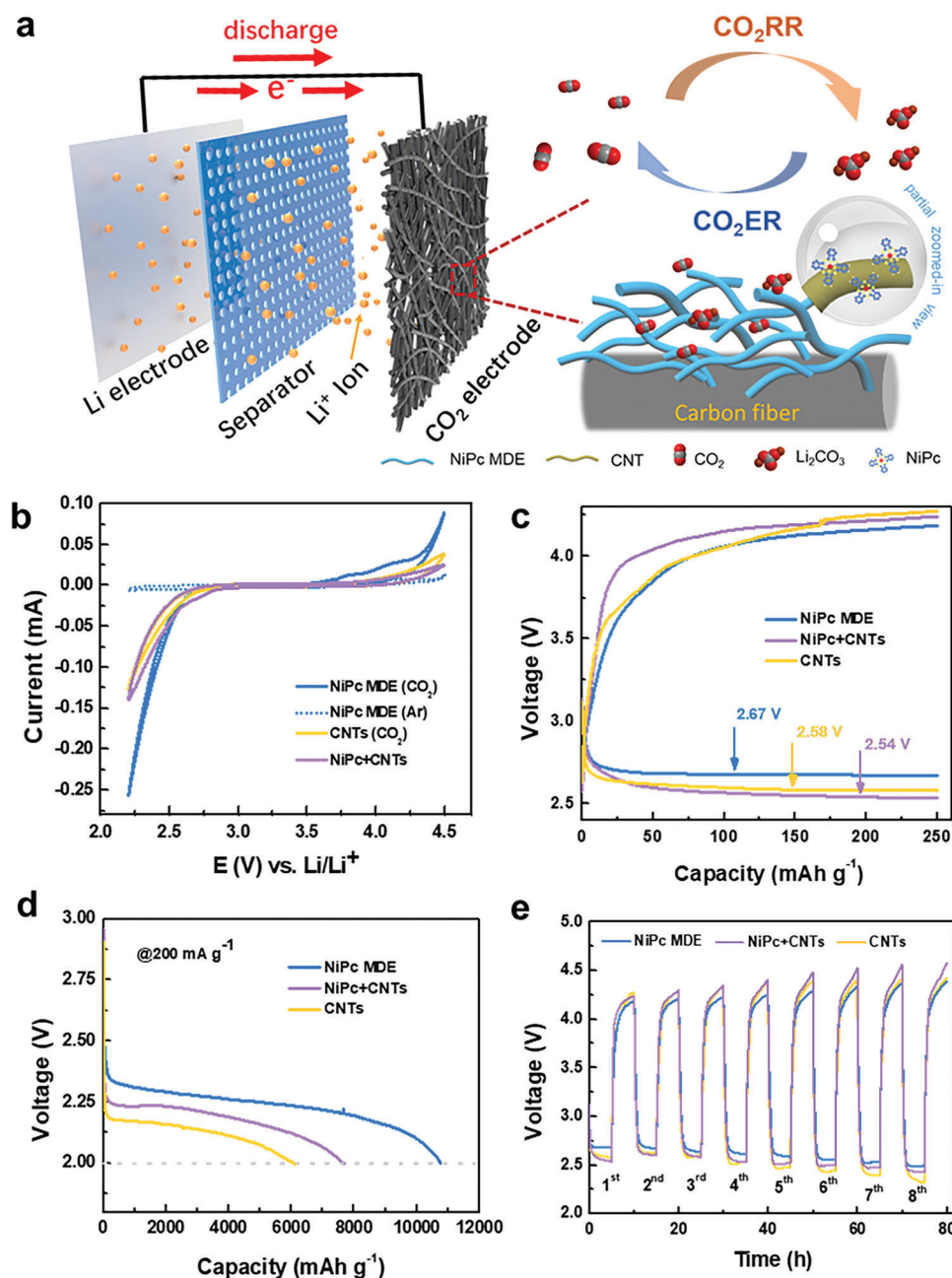
Figure 2. The cathode of Li-CO_2 batteries performance. a) Structures of the battery with NiPc MDE cathode. b) CV curves of the batteries with NiPc MDE, CNTs, and NiPc+CNTs cathode catalysts at a scan rate of 0.1 mV s^{-1}. c) The discharge–charge profiles of NiPc MDE, CNTs, and NiPc+CNTs cathode at 50 mA g^{-1}. d) Deep discharge curves of NiPc MDE, NiPc+CNTs, and CNTs cathode catalysts tested at 200 mA g^{-1}. e) Cycling performance tested at 50 mA g^{-1} of NiPc MDE catalyst.

at a current density of 50, 100, 200, and 400 mA g^{-1}, respectively, showing good rate performance and fast reaction kinetics due to the high conductivity and 3D network. Whereas NiPc MDE cathode could only run for 20 cycles, and the voltage gap enlarged quickly up to 2.30 V, ~~the Li~~ NiPc-CN MDE cathode could work stably for over 120 cycles with a voltage gap of 1.40 V at a current density of 50 mA g^{-1} (Figure 4d). Moreover, the stability of NiPc-CN MDE can be further proved by XANES measurements. The Ni L-edge (Figure S10, Supporting Information) exhibits negli-

gible change during battery operation. The comparison with the reported cathode catalysts illustrates the advantages of NiPc-CN MDE with enhanced activity and stability (Figures S11 and S12, and Table S2, Supporting Information).

To better understand the reversible CO_2 reduction and evolution reaction on the NiPc-CN MDE cathode, ex situ analysis techniques including SEM, XRD, EIS, and XPS were utilized to analyze the cathode at different stages (pristine, discharged, and charged). In **Figure 5**a(i), the pristine cathode exhibits unique

**ADVANCED
SCIENCE NEWS**

www.advancedsciencenews.com

NANO · MICRO
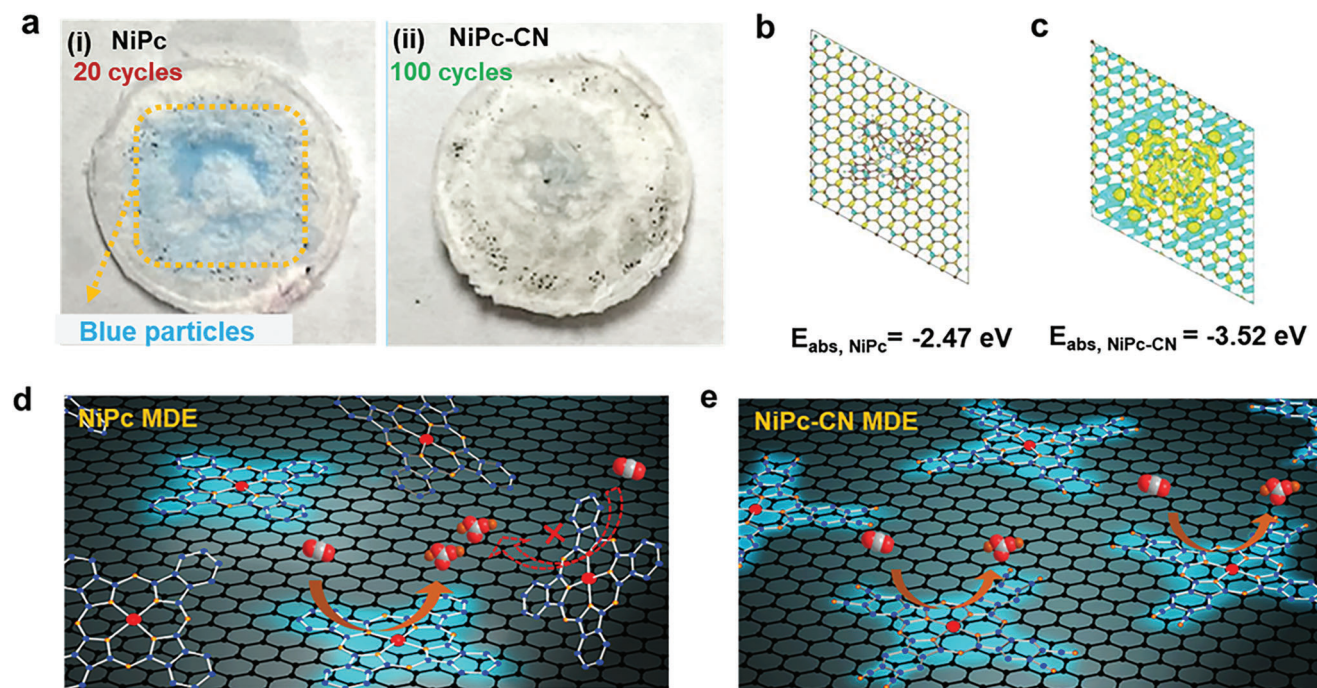
small

www.small-journal.com

Figure 3. Optimization of molecular electrocatalysts. a) The images of i) NiPc-MDE cathode after 20 cycles and ii) NiPc-CN MDE cathode after 100 cycles of operation at a current density of 50 mA g^{-1}. Charge density difference plot of b) NiPc and c) NiPc-CN supported on CNTs surface (single-layer graphene in modeling) with an isovalue of 0.0001. The absorption energy values are labeled below the corresponding plot. Schematic illustration of d) NiPc-MDE and e) NiPc-CN MDE in action as a Li-CO$_2$ battery cathode (the highlighted molecules indicate that they can be stabilized on the surface of CNTs).
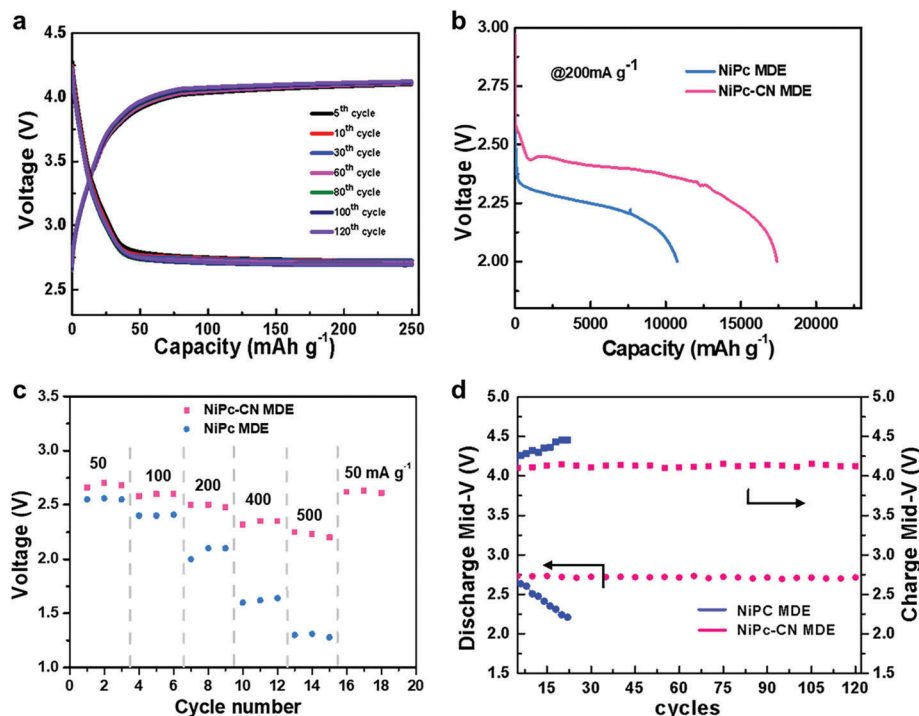

Figure 4. NiPc-CN MDE cathode performance. a) Discharge and charge profiles of the NiPc-CN MDE cathode were analyzed at a current density of 50 mA g^{-1} and a maximum capacity of 250 mAh g^{-1}. b) Full discharge profiles of NiPc-CN MDE and NiPc MDE tested at 200 mA g^{-1}. c) Rate performances of NiPc MDE and NiPc-CN MDE cathode within a limiting capacity of 800 mAh g^{-1} at various current densities. d) Long-term cycling curves of NiPc and NiPc-CN at 50 mA g^{-1}.
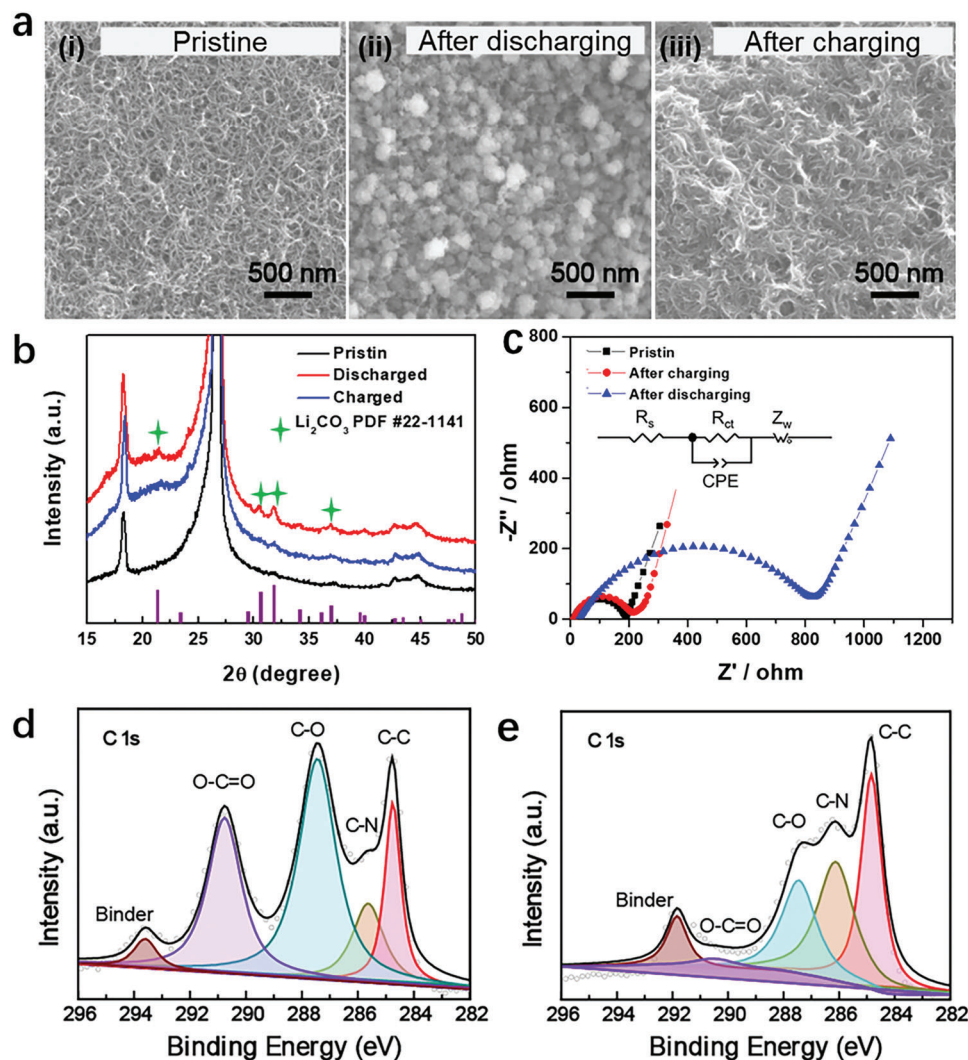
Figure 5. Reversibility of the NiPc-CN MDE cathode in Li–CO$_2$ batteries. a) SEM images of NiPc-CN MDE at different states: i) pristine, ii) after discharging, and iii) after charging. b) XRD patterns and c) Nyquist plots of Li–CO$_2$ batteries with NiPc-CN MDE cathodes at different stages (the inset is the equivalent circuit model for fitting the Nyquist plots). The XPS spectra of C1s at different states: d) discharged and e) charged.

3D porous morphology, ensuring sufficient space and sites for containing discharge products. After discharging, the particles of products were uniformly covered on the cathode surface, and the size of the particles is about 50–150 nm (Figure 5a(ii)). As the discharge depth increases, the amount of particles covered on the electrode gradually increases, also accompanied by the increase in size (Figure S13, Supporting Information). After subsequent charging to 4.2 V, the particles were almost decomposed to recover the porous nanotube network (Figure 5a(iii)). The reversible reaction is further confirmed by the XRD analysis, as shown in Figure 5b. New peaks at 21.2°, 30.5°, 31.6°, and 37.0° were detected after discharging, which are corresponding to the characteristic peaks of Li$_2$CO$_3$ crystals (PDF #22-1141). The discharge products at different discharge depths are all confirmed to be crystalline Li$_2$CO$_3$ (Figure S14, Supporting Information). And these peaks disappeared upon recharging. Notably, the reversible formation and decomposition of Li$_2$CO$_3$ on the cathode caused a significant change in battery impedance. As shown in Figure 5c

and Table S3, Supporting Information, the charge transfer resistance (R_{ct}) of the pristine NiPc-CN MDE electrode (178 Ω) experiences a significant increase after discharging (809 Ω). And then the conductivity of the electrode could be recovered and R_{ct} returns to its original value during the charging process, accompanied by the gradual decomposition of Li$_2$CO$_3$. The discharge–charge products were also analyzed by X-ray photoelectron spectroscopy (XPS), and the corresponding C 1s fine spectra were illustrated in Figures 5d,e. The peak at 290.7 eV can be assigned to the C=O of Li$_2$CO$_3$, formed during the discharge process. And this peak was significantly reduced after recharge due to the decomposing of Li$_2$CO$_3$. These investigations reveal that the NiPc-CN MDE has high activity in electron transfer, which can substantially facilitate the Li$_2$CO$_3$ formation and decomposition, thus effectively improving stability. To identify the composition of charge products during cycling, gas chromatography (GC) was carried out to determine the gases produced during the charging process in the Li-CO$_2$ battery with NiPc-CN MDE cathode. The

**ADVANCED
SCIENCE NEWS**

www.advancedsciencenews.com

NANO · MICRO

small

www.small-journal.com

experiments were performed by keeping Ar gas continuously taking into the GC detection during the charging process. It was observed that CO_2 is the only gas that evolved throughout the charging process (Figure S15, Supporting Information), and no evidence of other evolved gases (such as O_2, CO, and H_2) was observed. This qualitatively proved the reversibility of the Li-CO_2 battery.

3. Conclusion

In summary, this study investigates the performance of NiPc-based electrocatalysts as cathodes for Li-CO_2 batteries. By anchoring NiPc molecules on CNTs, the resulting MDE structure can efficiently catalyze CO_2 reduction and facilitate charging oxidation of Li_2CO_3 with the conductive and porous CNTs networks. The NiPc MDE demonstrates superior performance compared to aggregated NiPc. However, the weak molecule/CNTs interaction leads to NiPc detachment from CNTs in TEGDME electrolyte, reducing the stability of NiPc MDE in Li-CO_2 batteries. To address this, the molecule/CNTs interaction is enhanced through CN group modification, resulting in a stable NiPc-CN MDE cathode with high discharge voltage of 2.72 V and a small discharge–charge potential gap of 1.4 V. Experimental characterizations confirm the reversibility of Li_2CO_3 formation and decomposition during battery operation. This work demonstrates the potential of CNTs supported molecular catalysts for Li-CO_2 batteries.

4. Experimental Section

Materials Preparation: All the chemicals were bought commercially and used without purification, except when specified. NiPc was obtained from Alfa Aesar. NiPc-CN was synthesized using a slightly modified previously reported procedure.[24] Carbon paper (CFP, TGP-H-060) was obtained from Fuel Cell Store. The aqueous solutions were all prepared using Millipore water with a measured conductivity of 18.2 MΩ cm. CNTs from C-Nano (FT 9000) were purified by calcining in air at 500 °C for 5 h then washing with a 5 wt% HCl aqueous solution.

Preparation of MDE: To fabricate hybrid materials, 60 mg of purified CNTs was sonicated for 1 h in 60 mL DMF to disperse them. Subsequently, a specific amount of NiPc or NiPc-CN dissolved in DMF was added to the CNTs dispersion and mixed thoroughly by sonication for 45 min. To guarantee the uniform dispersion of the mixture, it was stirred at room temperature for 24 h. Thereafter, the precipitates were obtained by centrifugation of the mixture followed by washing three times with DMF and twice with ethanol. Finally, the precipitate was lyophilized to obtain the final product.

Material Characterizations: A range of analytical techniques were utilized to investigate the samples. TEM was conducted using an FEI Tecnai G2 F30 instrument. ICP-MS analyses were performed using an Agilent Technologies 7700 series instrument. XRD patterns were measured with a Rigaku MiniFlex-600 diffractometer using Cu Kα radiation ($\lambda = 1.5406$ Å) in an angle range of 10–60 (2θ) with a scanning rate of $2° \ min^{-1}$. SEM images were obtained using a Gemini LEO 1525 microscope and spectral analyses were conducted using a JEOL JSM 6400 SEM. EDS mappings were obtained using FEI Talos F200X instrument. Ultraviolet-visible spectrometry was performed with a Shimadzu UV3600 spectrometer. XPS was collected using a Physical Electronics Model 5700 instrument with a monochromatic Mg Kα X-ray source and calibrated with a C 1s peak (284.8 eV). XAS was collected using synchrotron radiation at Beamline 12 BM of the Advanced Photon Source in Argonne National Laboratory. Energy calibration was done through a reference nickel foil simultaneously measured. Athena and Artemis software packages were used to fit EXAFS spectra.

The Brunauer–Emmett–Teller (BET) surface areas were determined by N_2 adsorption isotherms at 77 K (Micromeritics ASAP 2460).

Electrode Preparation and Coin Cell Assembly: The Li-CO_2 battery assembly was constructed using CR2032 type (with holes) coin cells inside an argon-filled glovebox that had O_2 and H_2O levels below 1 ppm. Lithium metal served as the anode whereas 1 м lithium bis(trifluoromethane)sulfonimide (LiTFSI) in tetramethylene glycol dimethyl ether (TEGDME) (G4) was used as the electrolyte. Prior to the formation of the catalyst layer, the catalyst powder was dispersed uniformly in a mixture of NMP/EtOH (V:V = 4:1) to form a solution of 2.25 mg mL^{-1}. Next, sonication was carried out for 30 min as a means of assisting with the preparation of the solution. After this process, the solution was cast and dropped onto a circular carbon paper (1.12 cm^2, 0.2 mg) and was subsequently dried fully in a vacuum oven at 80 °C for 15 h. The coin cell was then connected to the battery tester for electrochemical testing, after being sealed inside a custom-built chamber filled with CO_2 at a pressure level of 1 atm.

Energy Density Calculation:

$$\text{energy density} \ \left(mAhg^{-1}\right) = \frac{\text{capacity (mAh)}}{\text{mass of cathode material (g)}} \quad (1)$$

where the mass of cathode material includes catalyst molecules and carbon nanotubes loaded on the substrate.

Supporting Information

Supporting Information is available from the Wiley Online Library or from the author.

Conflict of Interest

The authors declare no conflict of interest.

Data Availability Statement

The data that support the findings of this study are available from the corresponding author upon reasonable request.

[1] T. Senftle, E. Carter, *Acc. Chem. Res.* **2017**, *50*, 472.

[2] K. Sumida, D. Rogow, J. Mason, T. McDonald, E. Bloch, Z. Herm, T. Bae, J. Long, *Chem. Rev.* **2012**, *112*, 724.

[3] X. Duan, J. Xu, Z. Wei, J. Ma, S. Guo, S. Wang, H. Liu, S. Dou, *Adv. Mater.* **2017**, *29*, 1701784.

[4] B. Liu, Y. Sun, L. Liu, J. Chen, B. Yang, S. Xu, X. Yan, *Energy Environ. Sci.* **2019**, *12*, 887.

[5] Y. Qiao, J. Yi, S. Wu, Y. Liu, S. Yang, P. He, H. Zhou, *Joule* **2017**, *1*, 359.

[6] X. Li, J. Zhou, J. Zhang, M. Li, X. Bi, T. Liu, T. He, J. Cheng, F. Zhang, Y. Li, X. Mu, J. Lu, B. Wang, *Adv. Mater.* **2019**, *31*, 1903852.

[7] S. Xu, C. Chen, Y. Kuang, J. Song, W. Gan, B. Liu, E. Hitz, J. Connell, Y. Lin, L. Hu, *Energy Environ. Sci.* **2018**, *11*, 3231.

[8] Z. Xie, X. Zhang, Z. Zhang, Z. Zhou, *Adv. Mater.* **2017**, *29*, 1605891.

[9] C. Yang, K. Guo, D. Yuan, J. Cheng, B. Wang, *J. Am. Chem. Soc.* **2020**, *142*, 6983.

[10] Y. Hou, J. Wang, L. Liu, Y. Liu, S. Chou, D. Shi, H. Liu, Y. Wu, W. Zhang, J. Chen, *Adv. Funct. Mater.* **2017**, *27*, 1700564.

[11] J. Zhou, X. Li, C. Yang, Y. Li, K. Guo, J. Cheng, D. Yuan, C. Song, J. Lu, B. Wang, *Adv. Mater.* **2019**, *31*, 1804439.

[12] X. Li, H. Wang, Z. Chen, H. Xu, W. Yu, C. Liu, X. Wang, K. Zhang, K. Xie, K. Loh, *Adv. Mater.* **2019**, *31*, 1905879.

[13] Y. Xing, K. Wang, N. Li, D. Su, W. Wong, B. Huang, S. Guo, *Matter* **2020**, *2*, 1356.

[14] C. Wang, Q. Zhang, X. Zhang, X. Wang, Z. Xie, Z. Zhou, *Small* **2018**, *14*, 1800641.

[15] S. Yang, Y. Qiao, P. He, Y. Liu, Z. Cheng, J. Zhu, H. Zhou, *Energy Environ. Sci.* **2017**, *10*, 972.

[16] Y. Xing, Y. Yang, D. Li, M. Luo, N. Chen, Y. Ye, J. Qian, L. Li, D. Yang, F. Wu, R. Chen, S. Guo, *Adv. Mater.* **2018**, *30*, 1803124.

[17] Z. Zhang, C. Yang, S. Wu, A. Wang, L. Zhao, D. Zhai, B. Ren, K. Cao, Z. Zhou, *Adv. Energy. Mater.* **2019**, *9*, 1802805.

[18] S. Bie, M. Du, W. He, H. Zhang, Z. Yu, J. Liu, M. Liu, W. Yan, L. Zhou, Z. Zou, *ACS Appl. Mater. Interf* **2019**, *11*, 5146.

[19] Z. Zhang, X. Wang, X. Zhang, Z. Xie, Y. Chen, L. Ma, Z. Peng, Z. Zhou, *Adv. Sci.* **2018**, *5*, 1700567.

[20] S. Li, Y. Dong, J. Zhou, Y. Liu, J. Wang, X. Gao, Y. Han, P. Qi, B. Wang, *Energy Environ. Sci.* **2018**, *11*, 1318.

[21] Y. Liu, S. Zhao, D. Wang, B. Chen, Z. Zhang, J. Sheng, X. Zhong, X. Zou, S. Jiang, G. Zhou, H. Cheng, *ACS Nano* **2022**, *16*, 1523.

[22] C. Hu, L. Gong, Y. Xiao, Y. Yuan, N. Bedford, Z. Xia, L. Ma, T. Wu, Y. Lin, J. Connell, R. Shahbazian-Yassar, J. Lu, K. Amine, L. Dai, *Adv. Mater.* **2020**, *32*, 1907436.

[23] H. Yang, Q. Lin, C. Zhang, X. Yu, Z. Cheng, G. Li, Q. Hu, X. Ren, Q. Zhang, J. Liu, C. He, *Nat. Commun.* **2020**, *11*, 593.

[24] X. Zhang, Y. Wang, M. Gu, M. Wang, Z. Zhang, W. Pan, Z. Jiang, H. Zheng, M. Lucero, H. Wang, G. Sterbinsky, Q. Ma, Y. Wang, Z. Feng, J. Li, H. Dai, Y. Liang, *Nat. Energy* **2020**, *5*, 684.

[25] Y. Wu, Z. Jiang, X. Lu, Y. Liang, H. Wang, *Nature* **2019**, *575*, 639.

[26] J. Chen, K. Zou, P. Ding, J. Deng, C. Zha, Y. Hu, X. Zhao, J. Wu, J. Fan, Y. Li, *Adv. Mater* **2019**, *31*, 180548.

[27] J. Li, K. Zhang, Y. Zhao, C. Wang, L. Wang, L. Wang, M. Liao, L. Ye, Y. Zhang, Y. Gao, B. Wang, H. Peng, *Angew. Chem., Int. Ed.* **2020**, *61*, e202114612.

[28] X. Li, J. Zhang, G. Qi, J. Cheng, B. Wang, *Energy Storage Mater.* **2021**, *35*, 148.

[29] S. Liu, H. Yang, S. Hung, J. Ding, W. Cai, L. Liu, J. Gao, X. Liu, X. Ren, Z. Kuang, Y. Huang, T. Zhang, B. Liu, *Angew. Chem., Int. Ed.* **2020**, *59*, 798.

[30] X. Li, W. Bi, M. Chen, Y. Sun, H. Ju, W. Yan, J. Zhu, X. Wu, W. Chu, C. Wu, Y. Xie, *J. Am. Chem. Soc.* **2017**, *139*, 14889.

[31] H. Yang, S. Hung, S. Liu, K. Yuan, S. Miao, L. Zhang, X. Huang, H. Wang, W. Cai, R. Chen, J. Gao, X. Yang, W. Chen, Y. Huang, H. Chen, C. Li, T. Zhang, B. Liu, *Nat. Energy* **2018**, *3*, 140.

[32] Z. Zhang, Y. Wang, *J. Phys. Chem. C* **2021**, *125*, 13836.